PAPER

Check for updates

Multi-solvent large stopband monitoring based on the insolubility/superoleophilicity of PEDOT inverse opals†

Pingping Wu,[ab] Jingxia Wang [ID] *[ab] and Lei Jiang [ID] [ab]

Monitoring and post-processing of organic solvents are important for environmental protection. Challenges remain in the development of a universal material which can detect any solvent with a large stopband shift and show excellent stability. Herein, we demonstrate a poly 3,4-ethylenedioxythiophene inverse opal (PEDOT-IO) with a large stopband shift toward various solvents based on the insolubility/superoleophilicity properties. The PEDOT-IO film was fabricated by the potentiostatic polymerization of 3,4-ethylene dioxythiophene using a three-electrode system, infiltrating the interstices of the photonic crystal template with PEDOT and subsequently removing the template. The surface of the PEDOT-IO film presented a composite structure: interconnected pores and hollow shells. When the solvent was introduced into the voids of PEDOT-IO film, the effective refractive index (n) of the whole sample increased due to the replacement of air with the solvent, and the pores and hollow shells showed different degrees of swelling. The synergistic effect of increased n and volume expansion contributed to a large redshift of the stopband of the PEDOT-IO film. PEDOT-IO film exhibited excellent resistance to various solvents and high/low temperature. This work further enriches the application of conductive polymers in solvent-responsive PC sensors and provides a novel means of creating PC-based optical materials and devices.

1 Introduction

Responsive photonic crystals (PCs) are widely used in sensing,[1–5] displays,[6–9] anti-counterfeiting,[10–12] and other devices.[13–15] Their optical properties can be adjusted by physical or chemical methods, such as heat,[16,17] electricity,[18,19] magnetism,[20,21] *etc.*[16,22–29] With the rapid development of industry, organic solvents are widely used in chemical laboratories, the pharmaceutical industry, and daily life, which has seriously affected the environment and health.[4,30–32] Accordingly, monitoring and post-processing of organic solvents based on responsive PCs have been extensively researched by scientists.[31–33] Generally, there exist three types of solvent sensing PCs: single-,[25,32,34–37] homologous-,[38–42] and multi-solvent detection.[31,33,43] First, single solvent PC sensing was achieved based on the material responding to a specific solvent.[25,32,34–37] Second, homologous solvent detection was identified based on the special response properties of the PC framework, such as identification of

alcohols from block copolymers[38] and oil (alkanes) sensing from phenolic resins.[41] Third, multi-solvent PC detection was performed based on the swelling effect in various solvents,[43] such as framework swelling in various solvents,[31] or solvent infiltration with different polarities.[33] Among them, multi-solvent PC testing can be better for monitoring the leakage of organic solvents.[31,33,43] So far, multi-solvent PC sensing has achieved some important progress. For example, Wang *et al.* investigated multi-solvent sensing based on the morphology change of metal–organic inverse opals, but the stopband shift was small (<100 nm);[43] Yang *et al.* carried out multi-solvent detection using one-dimensional PCs based on the hydrogen bonding/solubility properties between the solvent and polymer;[31] Ge *et al.* developed multi-solvent sensing based on the dynamic reflection spectra of a PC gel, but the stopband shift of the PC was small (<100 nm) and irreversible based on the extraction of ethylene glycol.[33] At present, there are still some problems for multi-solvent PC sensing. Typically, the large stopband shift of PC can only target specific solvents, and the framework material collapses/breaks for other solvents, which causes poor reversibility. Therefore, challenges remain in the development of a universal PC material that can detect any solvent leakage (high-polarity, low-polarity, acidic, alkaline, strong or poor solubility solvents) with a large stopband shift and excellent reversible stability, achieving rapid visual monitoring of various solvents.

[a]*Key Laboratory of Bio-inspired Materials and Interfaces Sciences, Technique Institute of Physics and Chemistry, Chinese Academy of Sciences, Beijing, 100190, China*

[b]*Center of Material Science and Optoelectronics Engineering, School of Future Technologies, University of Chinese Academy of Sciences, Beijing, 100049, China. E-mail: jingxiawang@mail.ipc.ac.cn*

† Electronic supplementary information (ESI) available. See DOI: 10.1039/d1na00301a

The universal material (sensing framework) is the most critical part of solvent-responsive PC sensing.[30,44] Three conditions have to be met for the sensing framework to achieve multi-solvent detection: maintenance of stability in solvents; universal applicability to various solvents; and fast visualization. In recent years, various materials have been used as sensing elements of PCs, such as metals and metal oxides,[45] organic semiconductors,[46] and conductive polymers.[47–49] Compared with other materials, sensing devices prepared using conductive polymers and PC structures could increase the swelling degree and improve the sensitivity.[30,50–52] Among the conductive polymers, poly 3,4-ethylenedioxythiophene (PEDOT) is a bicyclic derivative of polythiophene with two alkoxy substituents attached to the 3 and 4 positions of the thiophene ring. PEDOT exhibits unprecedented air-, thermal- and solvent-stability based on the unique structure,[53] in which the electron-donating oxygen substituents stabilize free radicals and the six-membered ring closure extends the stabilization. At the same time, it has good electrical conductivity, high transparency and excellent environmental stability.[54,55] Therefore, PEDOT has great potential as a sensing element toward multi-solvent detection. However, to the best of our knowledge, no report is related to multi-solvent large stopband detection based on the PEDOT PC structure.

In this study, we present the first report of a PEDOT inverse opal (PEDOT-IO) with a large stopband shift toward a wide variety of solvents (high-polarity, low-polarity, acidic, alkaline, strong solubility or poor solubility solvents) based on the insolubility/superoleophilicity properties of PEDOT. PEDOT-IO film was fabricated by the potentiostatic polymerization of 3,4-ethylene dioxythiophene (EDOT) using a three-electrode system, infiltrating the PC template with PEDOT and subsequently removing the template. The surface of the PEDOT-IO film presented a composite structure based on non-uniform infiltration: interconnected pores and hollow shells. When the solvent was introduced into the voids of PEDOT-IO film, the effective refractive index (n) of the whole sample increased due to the replacement of air with the solvent, and the pores and hollow shells showed different degrees of swelling. The synergistic effect of increased n and volume expansion contributed to a large redshift of the stopband toward various solvents. In addition, PEDOT-IO film exhibits excellent resistance to various solvents, which is beneficial for multi-solvent detection without being damaged. This work further enriches the application of conductive polymers in solvent sensors and provides a novel means of creating PC-based optical materials and devices.

2 Experimental section

2.1 Materials

EDOT (purity 99.0%) was purchased from Aladdin Industrial Corporation and used without further purification. Sodium p-toluenesulfonate (TsONa) (purity 90.0%) was purchased from TCI (Shanghai, China) and used without further purification. Deionized water was used for potentiostatic polymerization. An indium tin oxide glass (ITO) working electrode with resistance less than 6 Ω was purchased from South China Science &

Technology Company Limited (Shenzhen, China). A platinum (Pt) electrode and saturated calomel electrode (SCE) were purchased from Tianjin Aida Hengsheng Technology Company Limited (Tianjin, China). All solvents were purchased from Sinopharm Chemical Reagent Company Limited and used without further purification.

2.2 Fabrication of the PC template

The PC template was prepared *via* vertically depositing the clean ITO glass substrate in a vial containing the P(St-MMA-AA) colloidal suspension at a concentration of 0.15 wt% at 60 °C and a relative humidity of 60% for 48 h.

2.3 Fabrication of PEDOT-IO film

PEDOT-IO film was manufactured by potentiostatic polymerization from an aqueous solution containing 0.02 M EDOT monomer and 0.1 M TsONa (electrolyte). The deposition was performed in a three-electrode system, with ITO as the working electrode, Pt as the counter electrode, and SCE as the reference electrode. A voltage of 1.0 V *versus* SCE was applied for the electrochemical deposition to ensure fast and homogeneous infiltration of the PEDOT into the interstices of the PC template in 5 min. After polymerization, the composite sample was rinsed with deionized water to remove the surface oligomers. The resulting PEDOT-IO film was obtained after removing the PC template by immersing the composite sample in THF for 2 h.

2.4 Solvent response behavior of PEDOT-IO film

A variety of solvents were dropped onto the surface of PEDOT-IO film. The PEDOT-IO film showed an obvious redshift of the stopband and color, and recovered to the original state after solvent evaporation.

2.5 Test of n of the PEDOT film in air and various solvents

Pure PEDOT film was produced on a silicon wafer by spin-coating the monomer 2,5-dibromo-3,4-ethylenedioxythiophene (100 mg mL^{-1} in chlorobenzene) with a spin speed of 3000 rpm for 30 s, and the sample was dried at 80 °C for 4 h. The n of PEDOT film in air and different solvents with a closed system was measured using the ellipsometer B-spline@632.8 nm mode.

2.6 Characterization

Electrochemical polymerization experiments were carried out using a CHI660D electrochemical workstation. All optical microscopy (OM) images were taken using a digital camera (Nikon, N1406 D7200). The reflection spectra were recorded using an Ocean Optics Maya 2000 PRO fiber optic spectrometer. The water contact angle (WCA) values were captured using a Dataphysics OCA-25 measurement system. Dynamic reflection spectra and CIE chromaticity diagrams were recorded using an Ocean Optics Maya 2000 PRO fiber optic spectrometer. The X-ray photoelectron spectroscopy (XPS) spectra were recorded using a Thermo Scientific ESCALAB250XI. The scanning electron microscopy (SEM) images were taken on a Thermo-4800

high-resolution field emission scanning electron microscope. The n of PEDOT film was taken using the ellipsometer B-spline@632.8 nm mode on a Woollam VASE M-2000V. Atomic force microscopy (AFM) images in air were taken on an LEXT OLS4500 Olympus. Liquid atomic force microscopy (L-AFM) images in solvents were taken on a MultiMode 8 Bruker.
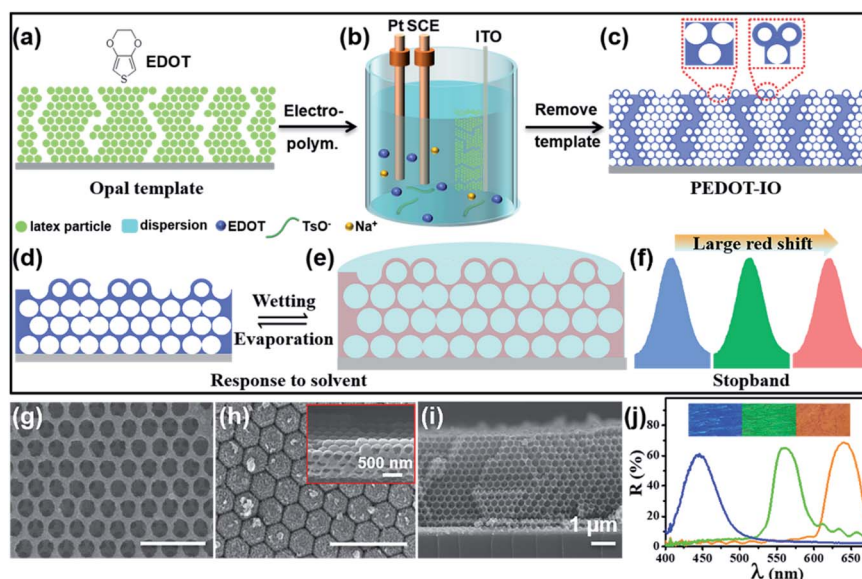
3 Results and discussion

3.1 Fabrication and characterization of PEDOT-IO film

Fig. 1 presents a schematic illustration of the fabrication and characterization of PEDOT-IO film.[18] As shown in Fig. 1a–c, PEDOT-IO film was prepared by potentiostatic polymerization, from an aqueous solution containing 0.02 M EDOT monomer and 0.1 M sodium p-toluenesulfonate (TsONa) (electrolyte) (Fig. S1†). The potentiostatic polymerization was carried out in a three-electrode system, with a PC template coated on ITO as the working electrode, Pt as the counter electrode, and SCE as the reference electrode (Fig. 1a).[18] Applying a potential of 1.0 V *versus* SCE for electrochemical deposition, PEDOT was introduced uniformly into the voids of the PC template in 5 min (Fig. 1b). After polymerization, the composite sample was rinsed with deionized water to remove surface oligomers. The bright PEDOT-IO film could be obtained after immersing the composite sample in tetrahydrofuran (THF) for 2 h to remove the PC template (Fig. 1c). Fig. 1d and e show the schematic illustrations of the complete infiltration/evaporation of the solvent toward PEDOT-IO film based on the superoleophilicity of the PEDOT framework. The solvent quickly infiltrated into the voids of the inverse opal solids, and the n of the whole

colloidal crystal increased due to the replacement of air with the solvent, leading to a large redshift of the stopband (Fig. 1f). The surface of PEDOT-IO film presented two composite structures: interconnected pores (Fig. 1g) and hollow shells (Fig. 1h). These two structures aroused from the gradient electro-polymerization infiltration process starting from the high conductivity toward the low conductivity part. In our system, the infiltration started from the sample close to the ITO substrate, and then transferred upward toward the whole PC template. Additionally, there are many cracks in the PC template assembled on the ITO substrate. The latex particles could be fully covered by electro-depositing a larger amount of PEDOT around the cracks owing to the strong conductivity, and the hollow shell structure easily formed from the cracked part after removing the PC template. In contrast, the interconnected pore structure was obtained after full infiltration of a small amount of PEDOT into the interstices of the regular assembled PC template and the subsequent removal of the template. Fig. 1g–i and S2† show the SEM images of the PEDOT-IO film, with a large-area, well-ordered structure (lattice spacing (d): pore, 258 nm; hollow shell, 270 nm), indicating the successful fabrication of the sample (thickness 4 μm). Furthermore, the stopband (λ) of the as-prepared sample could be modified from 450 to 643 nm, with the structure color changing from purple to red as shown in the inserted OM image (Fig. 1j and S3†).

3.2 Multi-solvent large stopband response of PEDOT-IO film

Fig. 2 and S4–S6† show the large stopband shift of PEDOT-IO film toward multiple solvents. The PEDOT-IO film presented

Fig. 1 Fabrication and characterization of PEDOT-IO film. (a–c) Schematic illustrations of the fabrication process of the PEDOT-IO film. (a) Opal template fabricated on the ITO substrate. (b) Set-up for electro-polymerization in the three-electrode system, with an ITO-coated PC template as the working electrode, Pt as the counter electrode, and SCE as the reference electrode. (c) Freshly made PEDOT-IO film. The top insets are structure schemes of the PEDOT-IO. (d and e) The complete infiltration/evaporation of the solvent toward PEDOT-IO film. (f) The large redshift of the stopband in response to the solvent. (g–i) SEM images of interconnected pores (g), hollow shell (h), and cross-section (i) of PEDOT-IO film. (j) UV-vis reflection spectra of PEDOT-IO film with various diameters. The top insets are OM images of the PEDOT-IO film with different structural colors.
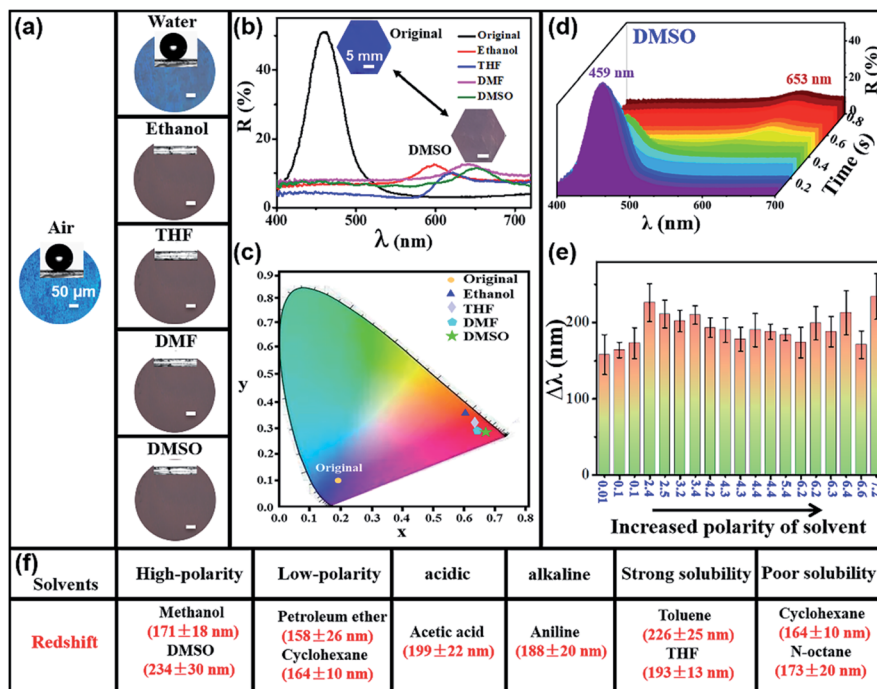
Fig. 2 Solvent response behavior of PEDOT-IO film. (a) OM images of PEDOT-IO film in air and in response to solvents. The insets are photos of solvent droplets on the surface of the sample. (b) Reflection spectra of PEDOT-IO film in its original state and in response to solvents. The insets in the upper-right corner are OM images of PEDOT-IO film in its original state and when immersed in DMSO. (c) CIE chromaticity diagram of PEDOT-IO film in its original state and in response to solvents. (d) Dynamic reflection spectra of PEDOT-IO film in response to DMSO. (e) Large redshift of the stopband of the PEDOT-IO film in response to various solvents with different polarities. (f) Summary of the large stopband of PEDOT-IO film with different types of solvents.

a large redshift of the stopband after the solvent penetrated into the sample. The sample returned to its original state after solvent evaporation. Fig. 2a and b present the changes of structural colors (OM images) and reflection spectra of PEDOT-IO film (blue; stopband, 459 nm) in water, ethanol, THF, N,N-dimethylformamide (DMF) and dimethyl sulfoxide (DMSO). The PEDOT-IO film exhibited hydrophobicity arising from the rough periodic structure. The sample remained blue when water was anchored on the surface of the PEDOT-IO film, indicating the non-infiltration of water into the PC structure. The superhydrophobicity/superoleophilicity of the film is a vital factor for multi-solvent sensing materials, which could effectively avoid the effect of water/humidity on the sensing process. In contrast, PEDOT-IO film showed a significant redshift of the stopband and the color changed from blue to red when organic solvents were dropped onto the film. This can be attributed to the superoleophilicity and rapid infiltration of the solvent into the -sample. Similarly, the stopbands of PEDOT-IO changed from 459 nm to 602, 621, 643, and 653 nm after dropping ethanol, THF, DMF, and DMSO respectively (Fig. 2a and b). This sensing process could be repeated at least 50 times without obvious damage to the PEDOT-IO film (Fig. S7†). Subsequently, a chromaticity diagram (CIE) was prepared to explore the achievable color gamut. The original sample was in the blue-violet region (x, y: 0.1903, 0.1038). The color slowly shifted to the red region and the corresponding chromaticity value also changed significantly when responding to organic solvents:

ethanol (x, y: 0.6123, 0.3609); THF (x, y: 0.6388, 0.3209); DMF (x, y: 0.6402, 0.2905); DMSO (x, y: 0.6693, 0.2891) (Fig. 2c). The corresponding color in the CIE diagram matched the observed color of the actual sample. Fig. 2d shows the dynamic reflection spectra of PEDOT-IO film in response to DMSO which reaches the maximum wavelength (653 nm) within 0.6 s. The intensity of the reflection peak gradually decreased and the stopband gradually shifted accompanied by DMSO penetration into the sample. The stopband remained stable at 653 nm after DMSO completely replaced the air pores. Fig. 2e presents the stopband shift of PEDOT-IO film with increasing solvent polarity (0.01 → 7.2). The reflection spectra were observed *in situ* by dropping various solvents on the surface of the PEDOT-IO film. The PEDOT-IO film showed a large redshift of the stopband (larger than 158 nm) toward solvents with different polarities. No linear relationship was observed between the stopband shift and the polarity of the solvent, but the PEDOT-IO film presented a higher stopband shift corresponding to solvents with suitable polarity, specifically, petroleum ether (polarity: 0.01, $\Delta\lambda$: 158 ± 26 nm), cyclohexane (polarity: 0.1, $\Delta\lambda$: 164 ± 10 nm), toluene (polarity: 2.4, $\Delta\lambda$: 226 ± 25 nm), xylene (polarity: 2.5, $\Delta\lambda$: 210 ± 18 nm), 1,2-dichloroethane (polarity: 3.2, $\Delta\lambda$: 202 ± 14 nm), dichloromethane (polarity: 3.4, $\Delta\lambda$: 210 ± 12 nm), THF (polarity: 4.2, $\Delta\lambda$: 193 ± 13 nm), ethyl acetate (polarity: 4.3, $\Delta\lambda$: 190 ± 16 nm), iso-propanol (polarity: 4.3, $\Delta\lambda$: 178 ± 16 nm), chloroform (polarity: 4.4, $\Delta\lambda$: 190 ± 22 nm), ethanol (polarity: 4.4, $\Delta\lambda$: 188 ± 10 nm), acetone (polarity: 5.4, $\Delta\lambda$: 184 ± 8 nm), acetonitrile
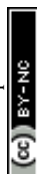
(polarity: 6.2, $\Delta\lambda$: 174 $\pm$ 20 nm), acetic acid (polarity: 6.2, $\Delta\lambda$: 199 $\pm$ 22 nm), aniline (polarity: 6.3, $\Delta\lambda$: 188 $\pm$ 20 nm), DMF (polarity: 6.4, $\Delta\lambda$: 213 $\pm$ 29 nm), methanol (polarity: 6.6, $\Delta\lambda$: 171 $\pm$ 18 nm), DMSO (polarity: 7.2, $\Delta\lambda$: 234 $\pm$ 30 nm). As shown in Fig. 2f, PEDOT-IO film showed a large stopband shift (>150 nm) toward various solvents, including solvents with polarity varying from 7.2 to 0.01 (DMSO (7.2), methanol (6.6), cyclohexane (0.1), petroleum ether (0.01)); an acidic solvent (acetic acid), or an alkaline solvent (aniline); a strong solubility solvent (toluene, THF) or a poor solubility solvent (cyclohexane, n-octane). It has never been reported in the literatures that PC film responds to such a wide variety of solvents with a large stopband shift.

3.3 Synergistic effect of increased n and volume expansion

The large stopband shift can be attributed to the synergistic effect of increased n and volume expansion. Fig. 3a and S8† show the comparison of the stopband shift between this work and literatures reports in response to solvents (cyclohexane, toluene, DCME, THF, ethyl acetate, ethanol, acetone, acetonitrile, DMF, DMSO). Compared with the previously reported literatures,[31,33,43] PEDOT-IO film showed a large stopband shift in response to various solvents. To understand the influencing mechanism, Fig. 3b, c and d present the relationship between the stopband shift of the PEDOT-IO film and n, the solubility parameter (δ) and the supporting electrolyte. The final redshift of the reflection spectra has a linear relationship with the n of the solvent, as shown in Fig. 3b. And the simulated straight line can be used to distinguish

different solvents ($\Delta\lambda = 300.9n - 228.4$).[41] Except for water, the redshift of the stopband of PEDOT-IO film increased with the enhanced n of the solvent. To verify the variation of the n of the sample in the solvent, we measured the n of pure PEDOT film in air and different solvents using the ellipsometer B-spline@632.8 nm mode. The n of the composite system increased with the increased n ($\bullet$) and δ ($\star$) of the solvents as shown in Fig. 3c and S9–S11.† Ethanol ($\Delta\lambda$, 188 $\pm$ 10 nm; δ, 18.1; n, 1.99 $\pm$ 0.026); THF ($\Delta\lambda$, 193 $\pm$ 13 nm; δ, 20.85; n, 2.01 $\pm$ 0.019); DMF ($\Delta\lambda$, 213 $\pm$ 29 nm; δ, 21.96; n, 2.07 $\pm$ 0.025); DMSO ($\Delta\lambda$, 234 $\pm$ 30 nm; δ, 24.65; n, 2.15 $\pm$ 0.017). There is a clear increase in the n of the sample in solvents compared with that in air (with n of 1.586). And the redshift of the stopband of PEDOT-IO film increased with the enhanced n and δ of the solvent. PEDOT-IO film with different electrolytes showed a similar large redshift of the stopband. Fig. 3d and S12–S14† show the relationship between the different supporting electrolytes and the redshift of the stopband of PEDOT-IO film such as lithium perchlorate (LiClO$_4$), sodium polystyrene sulfonate (PSS), 1-ethyl-3-methylimidazole bistrifluoromethanesulfonimide salt ((EMIm)NTf$_2$) and 1-methyl 3-butylimidazole tetrafluoroborate (BMIBF$_4$). The electrodeposition was also performed in a three-electrode system (Fig. 1a). PEDOT-IO films with different electrolytes were prepared by potentiostatic polymerization, from an aqueous solution containing 0.02 M EDOT monomer and 0.1 M supporting electrolytes (LiClO$_4$, PSS, (EMIm)NTf$_2$, BMIBF$_4$). A similar large stopband shift was observed for samples fabricated from different supporting electrolytes. The stopband
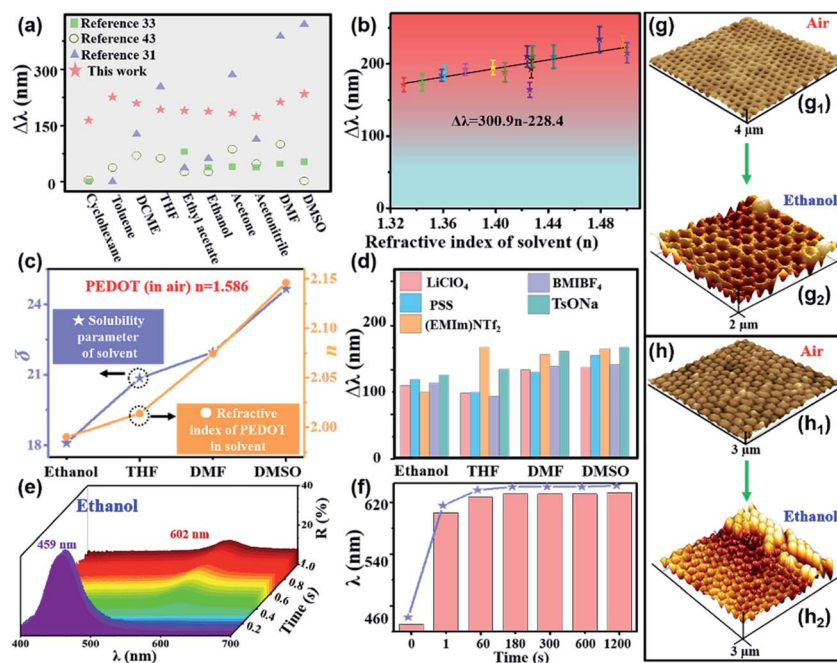

Fig. 3 Synergistic effect of increased n and volume expansion contributing to the large stopband shift. (a) The comparison of the stopband shift between this work and literature reports in response to solvents. (b) Relationship between the redshift of the stopband of the PEDOT–IO film and n of the solvent. (c) Summary of δ and n of PEDOT film in ethanol, THF, DMF, and DMSO. (d) Relationship between the redshift of the stopband of the PEDOT–IO film and supporting electrolyte. (e) Dynamic reflection spectra of PEDOT–IO film in response to ethanol. (f) Change of reflection spectra position with immersion time in ethanol. (g and h) AFM images of the pore (g$_1$ and g$_2$) and hollow shell (h$_1$ and h$_2$) structures in air and ethanol.
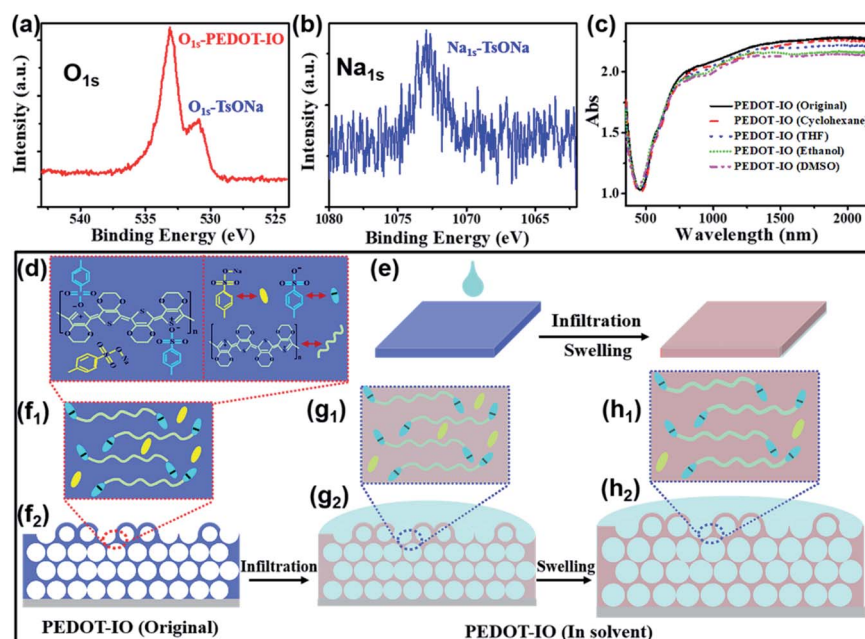
Table 1 Stopband shift of PEDOT-IO film resulting from the n of the solvent and volume expansion (ΔV)

Solvent	Pet. eth.	Cyc.	Tol.	Xyl.	1,2-Dic.	Dic.	THF	Eth. ace.	Iso-pro.	Chl.	Eth.	Ace.	Acet.	Ace. aci.	DMF	Met.	DMSO
$\Delta\lambda$ (experiment) nm	158 ± 26	164 ± 10	226 ± 25	210 ± 18	202 ± 14	210 ± 12	193 ± 13	190 ± 16	178 ± 16	190 ± 22	188 ± 10	184 ± 8	174 ± 20	199 ± 22	213 ± 29	171 ± 18	234 ± 30
$\Delta\lambda$ (n) nm	144	147	159	173	154	147	141	129	134	161	125	124	119	129	148	114	165
$\Delta\lambda$ (V) nm	14 ± 26	17 ± 10	66 ± 25	37 ± 18	48 ± 14	63 ± 12	52 ± 13	61 ± 16	44 ± 16	29 ± 22	63 ± 10	60 ± 8	55 ± 20	70 ± 22	65 ± 29	57 ± 18	69 ± 30

shifted 165 nm (LiClO$_4$), 178 nm (PSS), 150 nm ((EMIm)NTf$_2$), and 170 nm (BMIBF$_4$) in response to ethanol; the stopband shifted 148 nm (LiClO$_4$), 149 nm (PSS), 250 nm ((EMIm)NTf$_2$), and 140 nm (BMIBF$_4$) in response to THF; the stopband shifted 200 nm (LiClO$_4$), 194 nm (PSS), 235 nm ((EMIm)NTf$_2$), and 208 nm (BMIBF$_4$) in response to DMF; the stopband shifted 205 nm (LiClO$_4$), 232 nm (PSS), 247 nm ((EMIm)NTf$_2$), and 211 nm (BMIBF$_4$) in response to DMSO.

PEDOT-IO film showed obvious swelling after being immersed in organic solvents due to its unique chemical structure, which would greatly affect the large stopband shift.[47] Fig. 3e–g present the dynamic reflection spectra and volume expansion of PEDOT-IO film after being immersed in ethanol. The stopband shifted to the maximum wavelength (602 nm) within 0.6 s, and the intensity of the reflection peak gradually decreased accompanied by the penetration of ethanol into the sample. This shift of the stopband could be attributed to the increased n owing to solvent infiltration (Fig. 3e). And PEDOT-IO film could further swell to the equilibrium state after being immersed for a period of time, contributing to the further increased stopband shift. On further prolonging the observation time or adding the appropriate amount of solvent, the stopband continued to shift slightly until it reached equilibrium (631 nm) in 300 s. This shift results from the volume expansion after the air pores are completely replaced by the solvent (Fig. 3f, S15 and S16†). We characterized the volume change of PEDOT-IO film in air and ethanol by AFM and L-AFM, as shown in Fig. 3g and h.[31] It was found that the pore and hollow shell structures swelled to different degrees in the solvent system. The lattice spacing of the interconnected pore structure increased from 262 nm (in air) (Fig. 3g$_1$) to 290 nm (in ethanol) (Fig. 3g$_2$). The lattice spacing of the hollow shell structure increased from 285 nm (in air) (Fig. 3h$_1$) to 323 nm (in ethanol) (Fig. 3h$_2$). There was a greater expansion of the hollow shell (13.3%) compared with the interconnected pore structure (10.7%) in ethanol, contributing to a larger stopband shift. To understand what affected the stopband shift, we assumed the volume to be constant, and the stopband shift could be calculated according to the formula: $\lambda = 2d \times \varphi \times n_1 + 2d \times (1-\varphi) \times n_2$, where φ is the volume fraction of PEDOT; $n_1 = n_{PEDOT} = 1.586$; $n_2 = n_{Pore}$. The increased n brought about a stopband shift of more than 100 nm, and the residual stopband shift

Fig. 4 Chemical composition and mechanistic explanation of the large stopband shift of PEDOT-IO film. (a and b) XPS data for PEDOT-IO film. (c) Absorption spectra of PEDOT-IO film after being immersed in different solvents. (d) The structural formula of the PEDOT chain. (e–h) Schematic illustrations of the infiltration and expansion of the solvent toward the PEDOT-IO film.

might have resulted from volume swelling (Table 1 and Fig. S16†).

3.4 Mechanistic explanation of the large stopband shift of PEDOT-IO film

To clearly understand the large stopband shift of PEDOT-IO film, we summarized the mechanistic explanation based on the chemical composition of the PEDOT-IO film in Fig. 4a–h, S17 and S18.† The PEDOT-IO film (Fig. 4a and b) was super-oleophilic with the counter anion (TsO$^-$) doped in the PEDOT polymer chain, and a small amount of electrolyte salt (TsONa) mixed in the film, as could be confirmed from the two sets of oxygen peaks between 530 and 534 eV in the XPS spectra (Fig. 4a), originating from the oxygen atom (O1s) in the PEDOT chain (533 eV) and the counter anion (TsO$^-$) (531 eV) respectively.[56] The sodium atom (Na1s) at 1071 eV comes from a small amount of electrolyte salt (TsONa) mixed in the PEDOT-IO film during the electro-polymerization process (Fig. 4b).[18] Compared with the original state, the absorption spectra of PEDOT-IO film remained unchanged after being treated with different solvents, which indicated that the solvent response process did not change the doping state of the PEDOT-IO film (Fig. 4c and S18†).[56] Based on the above experimental data, Fig. 4d–h present a mechanistic explanation of the stopband shift of PEDOT-IO film. PEDOT is a linear polymer composed of rigid elements with ether bonds in polar groups. It presents super-oleophilicity and contributes to rapid spreading or penetration of the solvent into the PEDOT-IO structure (Fig. 4d). In addition, the polar solvent can swell the polymer film thereby increasing the distance between the polymer chains and the counter anion.[47] Therefore, the large stopband shift of PEDOT-IO film in response to solvents can be attributed to the solvent replacement of air pores and the volume expansion (Fig. 4e–h). The PEDOT-IO film was doped with TsO$^-$ and mixed with TsONa (Fig. 4f). The solvent would rapidly penetrate into the pore structure and replace the air pores after solvent dropping into the film, which contributed to the increased n and the large redshift of the stopband (Fig. 4g). Then, the polar solvent could further swell the film and cause volume expansion of PEDOT and an increased redshift of the stopband. And the TsONa mixed in the film could be removed during dropping/evaporation of the solvent (Fig. 4h).

3.5 Stability of the PEDOT-IO film

PEDOT is an insoluble and infusible conductive polymer with excellent stability at various temperatures and in liquid environments. These features prevent the destruction or collapse of the sample, ensuring its potential application for multi-solvent sensing. Fig. 5 shows the stability of the PEDOT-IO film towards friction loss, high/low temperature and various solvents. The sandpaper friction loss experiment device was made as follows: taking a piece of grit sandpaper (1.0 × 1.0 cm) glued to a weight with a mass of 5 g; keeping a constant pressure (about 500 Pa) on the abrasion area, with the pressure calculated from $P = F/S = mg/S$, where P is the pressure; F is the force; S is the force area; m is the mass; g is 9.8 N kg^{-1} (Fig. 5a$_1$).
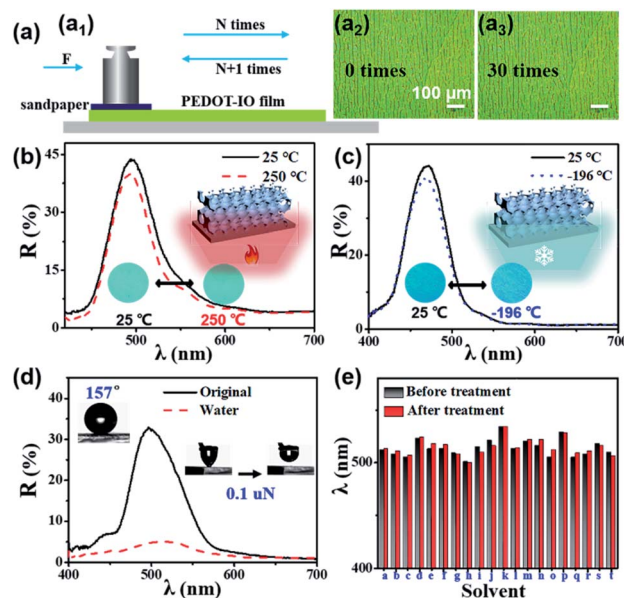

Fig. 5 The stability of PEDOT-IO film. (a$_1$) The sandpaper friction loss experiment device. OM images of the PEDOT-IO film before (a$_2$) and after (a$_3$) rubbing 30 times. (b) OM images and reflection spectra of PEDOT-IO film at 25 °C and heated to 250 °C. (c) OM images and reflection spectra of PEDOT-IO film at 25 °C and cooled to −196 °C. (d) Reflection spectra of PEDOT-IO film in response to water. The inset in the upper-left corner is the photo of a water droplet on the surface of the sample, and the insets on the right are photos of a water droplet before and after leaving the surface of the sample. (e) Summary of reflection spectra changes before and after immersion in various solvents.

On placing sandpaper with a weight on the surface of the PEDOT-IO film and moving it back and forth in parallel for 30 cycles, no obvious damage occurred on the surface of the sample. And the surface structure of the sample began to break after rubbing for 50 cycles (every 5 cycles, using N$_2$ to blow off the surface residue) (Fig. 5a$_2$, a$_3$ and S19†). The PEDOT-IO film also shows excellent high/low temperature stability. The OM images and reflection spectra of the PEDOT-IO film remained unchanged when the sample was heated to 250 °C or cooled to −196 °C (Fig. 5b, c and S20–S22†). In addition, the PEDOT-IO film exhibited superhydrophobicity in air (WCA, 157°; dynamic adhesion force, 0.1 μN). The structural color of the PEDOT-IO film remained unchanged with water droplets anchored on the surface of the sample (Fig. 2a). There is a slight stopband shift (498 → 510 nm), accompanied by a significant decrease in reflectivity resulting from the water covering the sample (Fig. 5d). Fig. 5e, S23 and S24† summarize the OM images and reflection spectra of PEDOT-IO film before and after immersion in various solvents. The PEDOT-IO film presented excellent solvent resistance, and the inverse opal structure remained stable with unchanged structural color/reflectance spectra after treatment with various solvents.

3.6 The volatile organic solvent sensing of PEDOT-IO film

Fig. 6 shows the PEDOT-IO film used for monitoring volatile solvents. As shown in Fig. 6a, the volatile organic solvent
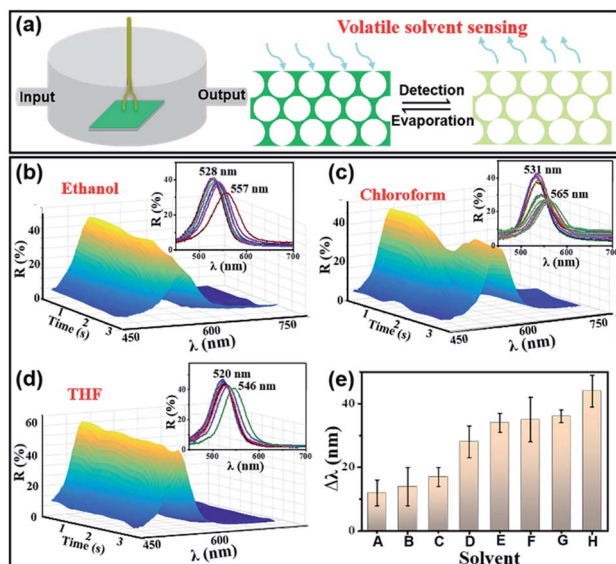
Fig. 6 The volatile solvent sensing of PEDOT-IO film. (a) The volatile organic solvent detection device. (b–d) Dynamic reflection spectra of PEDOT-IO film in response to ethanol (b), chloroform (c), and THF (d). (e) Summary of the detection of various volatile organic solvents.

detection device was in a closed system.[4,30] The PEDOT-IO film was placed at the bottom of the device, and a spectrometer was connected for *in situ* monitoring of reflection spectra. The volatile organic solvent entered the closed device from one end of the device. When the sample sensed the organic gas, there was a rapid redshift of the stopband. The sample returned to the initial state after steam evaporation (Fig. 6a). Fig. 6b, c and d show the dynamic reflection spectra upon entry of ethanol, chloroform, and THF, respectively. The color (reflection spectra) of the sample changed from green (528 nm) to yellow-green (557 nm) within 2.8 s when ethanol entered the device. The color (reflection spectra) of the sample changed from green (531 nm) to yellow-green (565 nm) within 2.2 s when chloroform entered the device. The color (reflection spectra) of the sample changed from green (520 nm) to yellow-green (546 nm) within 3.0 s when THF entered the device. Fig. 6e and S25† summarize the detection behavior of the sample toward various volatile solvents. The redshift of the stopband was 12 ± 4 nm (A—hexane, 2.4 s), 14 ± 6 nm (B—petroleum ether, 3.0 s), 17 ± 3 nm (C—cyclohexane, 3.5 s), 28 ± 5 nm (D—THF, 3 s), 34 ± 3 nm (E—chloroform, 2.2 s), 35 ± 7 nm (F—ethanol, 2.8 s), 36 ± 2 nm (G—acetone, 2.0 s), and 44 ± 5 nm (H—acetonitrile, 1.8 s), respectively. The above results indicated that the PEDOT-IO film had potential applications as a sensor for monitoring volatile solvents.

4 Conclusions

We fabricated a PEDOT-IO film with multi-solvent and large stopband monitoring based on the synergistic effect of the increased n and volume expansion. The surface of the PEDOT-IO film presented a composite structure: interconnected pores and hollow shells. When the solvents were dropped onto the

PEDOT-IO film, the n of the whole sample increased, and the pores and hollow shells showed different degrees of swelling. The synergistic effect of increased n and volume expansion contributed to a large redshift of the stopband. This work enriches the application of conductive polymers in solvent sensing PCs and provides a novel means of creating PC-based optical materials and devices.

Author contributions

Pingping Wu: conceptualization, methodology, investigation, data curation, and writing – original draft. Jingxia Wang: conceptualization, supervision, and writing – review and editing. Lei Jiang: supervision.

Conflicts of interest

There are no conflicts to declare.

Acknowledgements

References

1 Z. Chen, Y. Yu, J. Guo, L. Sun and Y. Zhao, *Adv. Funct. Mater.*, 2020, **31**, 2007527.

2 D. Kou, W. Ma and S. Zhang, *Adv. Funct. Mater.*, 2020, **31**, 2007032.

3 S. Li, Y. Zeng, W. Hou, W. Wan, J. Zhang, Y. Wang, X. Du and Z. Gu, *Mater. Horiz.*, 2020, **7**, 2944–2950.

4 D. Kou, Y. Zhang, S. Zhang, S. Wu and W. Ma, *Chem. Eng. J.*, 2019, **375**, 121987.

5 C. Xiong, Y. Lan, B. Chen, Z. Li, Y. Zhang and Y. Song, *J. Mater. Chem. C*, 2020, **8**, 12800–12805.

6 B. B. Patel, D. J. Walsh, D. H. Kim, J. Kwok, B. Lee, D. Guironnet and Y. Diao, *Sci. Adv.*, 2020, **6**, eaaz7202.

7 Y. Wang, Q. Zhao and X. Du, *Mater. Horiz.*, 2020, 7, 1341–1347.

8 Y. Tian, Z. Zhu, Q. Li, J. Zhang, C. F. Wang, G. Wu, S. S. Li, J. J. Xiao and S. Chen, *Chem. Eng. J.*, 2020, **415**, 128950.

9 J. Liao, C. Zhu, B. Gao, Z. Zhao, X. Liu, L. Tian, Y. Zeng, X. Zhou, Z. Xie and Z. Gu, *Adv. Funct. Mater.*, 2019, **29**, 1902954.

10 Y. Qi, L. Chu, W. Niu, B. Tang, S. Wu, W. Ma and S. Zhang, *Adv. Funct. Mater.*, 2019, **29**, 1903743.

11 Y. Liu, L. Shang, H. Wang, H. Zhang, M. Zou and Y. Zhao, *Mater. Horiz.*, 2018, **5**, 979–983.

12 J. Hou, H. Zhang, B. Su, M. Li, Q. Yang, L. Jiang and Y. Song, *Chem.–Asian J.*, 2016, **11**, 2680–2685.

13 Y. Yang, Y. Chen, Z. Hou, F. Li, M. Xu, Y. Liu, D. Tian, L. Zhang, J. Xu and J. Zhu, *ACS Nano*, 2020, **14**, 16057–16064.

14 C. Wang, X. Lin, C. G. Schäfer, S. Hirsemann and J. Ge, *Adv. Funct. Mater.*, 2020, **31**, 2008601.

15 P. Wu, J. Wang and L. Jiang, *Mater. Horiz.*, 2020, **7**, 338–365.

16 Z. Zhang, Z. Chen, Y. Wang and Y. Zhao, *Proc. Nati. Acad. Sci. U.S.A.*, 2020, **117**, 18310–18316.

17 X. Li, D. Zhao, K. J. Shea, X. Li and X. Lu, *Mater. Horiz.*, 2021, **8**, 932–938.

18 P. Wu, J. Guo, K. Jiang, J. Wang and L. Jiang, *Adv. Funct. Mater.*, 2019, **29**, 1808473.

19 K. Chen, Q. Fu, S. Ye and J. Ge, *Adv. Funct. Mater.*, 2017, **27**, 1702825.

20 L. Kong, Y. Feng, W. Luo, F. Mou, K. Ying, Y. Pu, M. You, K. Fang, H. Ma and J. Guan, *Adv. Funct. Mater.*, 2020, **30**, 2005243.

21 H. Kim, J. Ge, J. Kim, S. Choi, H. Lee, H. Lee, W. Park, Y. Yin and S. Kwon, *Nat. Photo.*, 2009, **3**, 534–540.

22 M. M. Ito, A. H. Gibbons, D. Qin, D. Yamamoto, H. Jiang, D. Yamaguchi, K. Tanaka and E. Sivaniah, *Nature*, 2019, **570**, 363–367.

23 Y. Wang, D. Aurelio, W. Li, P. Tseng, Z. Zheng, M. Li, D. L. Kaplan, M. Liscidini and F. G. Omenetto, *Adv. Mater.*, 2017, **29**, 1702769.

24 J. H. Kim, G. H. Lee, J. B. Kim and S. H. Kim, *Adv. Funct. Mater.*, 2020, **30**, 2001318.

25 Y. Hu, D. Yang and S. Huang, *Adv. Optical Mater.*, 2020, **8**, 1901541.

26 R. Chen, D. Feng, G. Chen, X. Chen and W. Hong, *Adv. Funct. Mater.*, 2021, **31**, 2009916.

27 Y. Q. Zhang, Q. Q. Fu and J. P. Ge, *Small*, 2017, **13**, 1603351.

28 Y. Li, Q. Fan, X. Wang, G. Liu, L. Chai, L. Zhou, J. Shao and Y. Yin, *Adv. Funct. Mater.*, 2021, **31**, 2010746.

29 Y. Wang, X. Cao, J. Cheng, B. Yao, Y. Zhao, S. Wu, B. Ju, S. Zhang, X. He and W. Niu, *ACS Nano*, 2021, **15**, 3509–3521.

30 Q. Zhong, H. Xu, H. Ding, L. Bai, Z. Mu, Z. Xie, Y. Zhao and Z. Gu, *Colloids Surf., A*, 2013, **433**, 59–63.

31 Z. Wang, J. Zhang, J. Li, J. Xie, Y. Li, S. Liang, Z. Tian, C. Li, Z. Wang, T. Wang, H. Zhang and B. Yang, *J. Mater. Chem.*, 2011, **21**, 1264–1270.

32 Y. L. Ko, H. P. Tsai, K. Y. Lin, Y. C. Chen and H. T. Yang, *J. Colloid Interface Sci.*, 2017, **487**, 360–369.

33 Y. Zhang, Q. Fu and J. Ge, *Nat. Commun.*, 2015, **6**, 7510.

34 C. Sun, D. Zhu, H. Jia, C. Yang, Z. Zheng and X. Wang, *ACS Appl. Mater. Interfaces*, 2020, **12**, 26455–26463.

35 K. Zhong, J. Li, L. Liu, S. V. Cleuvenbergen, K. Song and K. Clays, *Adv. Mater.*, 2018, **30**, 1707246.

36 L. Bai, Z. Xie, W. Wang, C. Yuan, Y. Zhao, Z. Mu, Q. Zhong and Z. Gu, *ACS Nano*, 2014, **8**, 11094–11100.

37 Y. Fang, Y. Ni, B. Choi, S.-Y. Leo, J. Gao, B. Ge, C. Taylor, V. Basile and P. Jiang, *Adv. Mater.*, 2015, **27**, 3696–3704.

38 D. P. Song, T. H. Zhao, G. Guidetti, S. Vignolini and R. M. Parker, *ACS Nano*, 2019, **13**, 1764–1771.

39 L. Duan, B. You, S. Zhou and L. Wu, *J. Mater. Chem.*, 2011, **21**, 687–692.

40 E. P. A. Heeswijk, L. Yang, N. Grossiord and A. P. H. J. Schenning, *Adv. Funct. Mater.*, 2019, **30**, 1906833.

41 H. Li, J. Wang, L. Yang and Y. Song, *Adv. Funct. Mater.*, 2008, **18**, 3258–3264.

42 I. B. Burgess, L. Mishchenko, B. D. Hatton, M. Kolle, M. Loncar and J. Aizenberg, *J. Am. Chem. Soc.*, 2011, **133**, 12430–12432.

43 J. Liu, J. Liu, P. Wu, M. Zhang, J. Wang and L. Jiang, *J. Photochem. Photobiol., A*, 2018, **355**, 125–130.

44 Y. N. Wu, F. Li, W. Zhu, J. Cui, C. A. Tao, C. Lin, P. M. Hannam and G. Li, *Angew. Chem., Int. Ed.*, 2011, **50**, 12518–12522.

45 M. E. Franke, T. J. Koplin and U. Simon, *Small*, 2006, **2**, 36–50.

46 E. Comini, G. Faglia, G. Sberveglieri, Z. Pan and Z. L. Wang, *Appl. Phys. Lett.*, 2002, **81**, 1869–1871.

47 H. Bai and G. Shi, *Sensors*, 2007, **7**, 267–307.

48 X. Guo and A. Facchetti, *Nat. Mater.*, 2020, **19**, 922–928.

49 U. Lange, N. V. Roznyatovskaya and V. M. Mirsky, *Anal. Chim. Acta*, 2008, **614**, 1–26.

50 L. Jin, Y. Zhao, X. Liu, Y. Wang, B. Ye, Z. Xie and Z. Gu, *Soft Matter*, 2012, **8**, 4911.

51 T. Kuno, Y. Matsumura, K. Nakabayashi and M. Atobe, *Angew. Chem., Int. Ed.*, 2016, **55**, 2503–2506.

52 L. Xu, J. Wang, Y. Song and L. Jiang, *Chem. Mater.*, 2008, **20**, 3554–3556.

53 I. Petsagkourakis, N. Kim, K. Tybrandt, I. Zozoulenko and X. Crispin, *Adv. Electron. Mater.*, 2019, **5**, 1800918.

54 S. Kirchmeyer and K. Reuter, *J. Mater. Chem.*, 2005, **15**, 2077–2088.

55 T. Darmanin and F. Guittard, *Prog. Polym. Sci.*, 2014, **39**, 656–682.

56 R. Chen, S. Chen, Y. Zhou, Z. Wei, H. Wang, Y. Zheng, M. Li, K. Sun and Y. Li, *Macromolecules*, 2020, **53**, 4247–4254.